Plasma Phys. Control. Fusion **51** (2009) 055001 (19pp) doi:10.1088/0741-3335/51/5/055001

Fast ion D_α imaging in the DIII-D tokamak

M A Van Zeeland[1], W W Heidbrink[2] and J H Yu[3]

[1] General Atomics, PO Box 85608, San Diego, CA 92186-5608, USA
[2] University of California-Irvine, 4129 Frederick Reines Hall, Irvine, CA 92697, USA
[3] University of California-San Diego, 9500 Gilman Drive, La Jolla, CA 92093, USA

E-mail: vanzeeland@fusion.gat.com

Received 30 September 2008, in final form 29 January 2009
Published 26 February 2009
Online at stacks.iop.org/PPCF/51/055001

Abstract
Doppler shifted fast ion D_α light (FIDA) emitted by neutralized energetic ions is imaged in the DIII-D tokamak using a fast framing camera in conjunction with a narrowband interference filter. Both the 2D spatial structure and temporal evolution of the FIDA emission are in agreement with Monte Carlo simulations assuming classical energetic ion slowing down. This technique can be used to obtain 2D energetic ion profile information in fusion plasmas.

(Some figures in this article are in colour only in the electronic version)

1. Introduction

In addition to thermal ions, non-thermal distributions of energetic ions (fast ions) are often present in tokamak experiments, being created through a variety of processes, some of which are fusion reactions, high energy neutral beam injection and RF wave acceleration. Fast ions can be a major source of energy, momentum and particles for the plasma, indeed in future fusion reactors the fusion generated alpha particles will be required to slow down on thermal particles in order to sustain the thermonuclear burn. For these reasons the study of fast ion confinement and transport is a fundamental topic that must be supported with detailed experimental measurements such as those made possible by the recently developed technique [1] of fast ion D_α (FIDA) spectroscopy.

FIDA spectroscopy measures the Doppler shifted D_α spectrum produced by neutralized fast ions (reneutrals or fast neutrals) born in charge-exchange events with injected neutrals and halo neutrals. Previously, several vertical viewing FIDA channels were implemented on DIII-D, and each channel was equipped with a dedicated spectrometer for detailed analysis of the emitted spectra in the D_α range [2, 3]. By selecting a wavelength of the emission spectrum, the fast neutral parallel velocity along the line of sight (LOS) is selected and energy discrimination is obtained; essentially, the measured D_α photon that has been Doppler shifted due to motion toward the

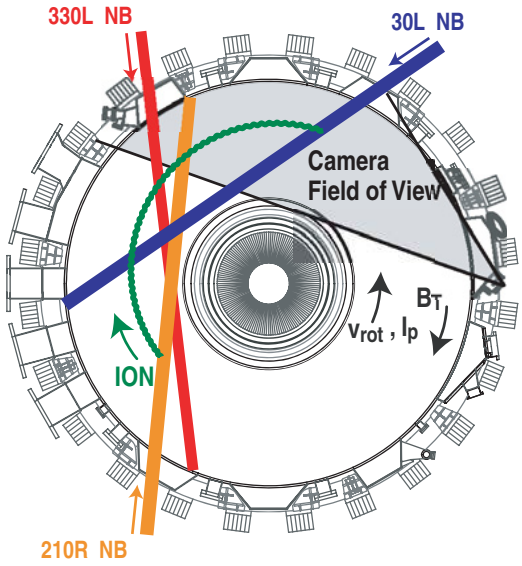

Figure 1. Plan view of the DIII-D tokamak showing the camera viewing region—grey. Arrows indicate the direction of toroidal field (B_T), plasma current (I_p), toroidal rotation (v_{rot}) and neutral beam injection. Individual neutral beams 330L (co-current), 210R (counter-current) and 30L (co-current, imaging beam) are labelled. The width of beam trajectory lines represents the approximate width of each injected-neutral plume in the horizontal plane.

collection optics must match the selected wavelength. Recent incarnations of FIDA spectroscopy forgo the dedicated spectrometer and use photodetectors in combination with narrowband interference filters chosen *a priori* to correspond to a given energy range [4].

This paper presents work which further extends FIDA spectroscopy to include 2D time resolved imaging. A narrowband interference filter is used in conjunction with a tangentially viewing 12-bit fast framing Phantom V7.1 CMOS camera [5] to create 2D movies of the FIDA emission profile, a technique called fast ion D_α imaging (FIDAI). Both the spatial structure and temporal evolution of the FIDA emission, during a specifically designed FIDA/FIDAI validation experiment on DIII-D are in excellent agreement with Monte Carlo simulations assuming classical beam ion slowing down.

2. Experimental setup

Figure 1 shows a plan view of the DIII-D tokamak midplane as well as the focal plane of the fast framing camera and viewable region (shaded grey). The semi-tangential view spans from the inner wall on the high field side (HFS) to the outer wall on the low field side (LFS). The spatial resolution of the detector is 384 × 256 pixels with 1 pixel imaging 0.05–0.2 cm^2 at the point of tangency, where the exact size depends on the location within the field of view. The number of usable pixels depends on the camera frame rate which was fixed at 300 frames s^{-1} for the study presented here; however, the camera itself is capable of imaging at up to 120 kframes s^{-1}. Taking advantage of this large bandwidth and dynamic range the same camera has been used recently to provide detailed measurements of tearing modes through imaging of visible bremsstrahlung emission (VBE) [6, 7] as well as cold edge

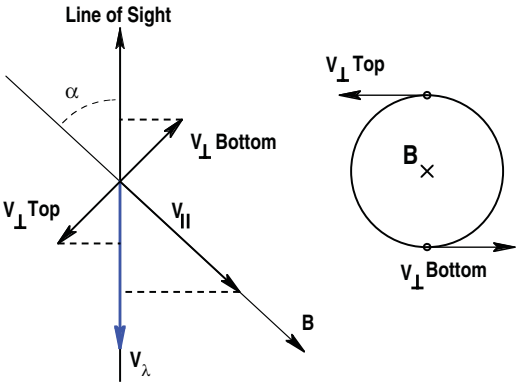

Figure 2. Sketch showing how the range of ion velocities immediately preceding neutralization can satisfy the nominal filter bandpass condition, i.e. the component of $v_{\rm ion}$ antiparallel to pixel LOS must equal filter bandpass velocity (v_λ). Ion velocity perpendicular/parallel to the local magnetic field is $v_\perp/v_\parallel$, respectively. The angle between the pixel LOS and the local magnetic field at the point of neutralization is α.

D_α imaging of fast transient events such as edge localized modes (ELMs) [5]. Also shown in figure 1 are trajectories of the relevant 78–81 keV neutral beam lines along with their injection direction as well as the direction of toroidal field ($B_{\rm T}$), plasma current ($I_{\rm p}$) and toroidal rotation ($v_{\rm rot}$).

The camera images light with wavelengths in the entire visible range which can be from any variety of sources. As discussed in the introduction, to restrict the light to that in the FIDA range, a narrowband interference filter is used with an approximate normal incidence passband centered at $\lambda_{\rm c} = 653.2687$ nm with full-width to the $1/e$ transmission points of 4.2 nm. This band corresponding to blue shifted D_α ($\lambda_{D_\alpha 0} = 656.1$ nm) was chosen as to avoid emission from excited neutrals injected directly by the 30L neutral beam (imaging beam), and in practice, is tilted to further shift the passband to the blue and avoid other interferences. Some blue shifted emission from excited neutrals injected directly by the 330L can make it through the filter and will be discussed in section 5. The other primary sources of emission in this wavelength region are halo (thermal) neutrals formed by charge exchange events with plasma deuterons, VBE, and reneutrals (the source of interest) formed by charge exchange events with circulating fast ions. An example fast ion trajectory that could contribute to the camera signal is shown as a green overlaid curve in figure 1. This particular ion corresponds to a counter-current going 30 keV particle with $V_\parallel/|V| = -0.8$ generated by the 210R NB that re-neutralizes on the 30L neutral plume. These sources and the implications of each are all discussed in detail in [2] and the calculated relative contributions of each for the discharge presented here will be discussed in section 5. The actual FIDA photon flux arriving at a pixel (I) is roughly proportional to $n_{\rm fi} n_{\rm neut}\, {\rm d}L$, where $n_{\rm fi}$ is the fast ion density satisfying the filter passband (described below), $n_{\rm neut}$ is the deuterium neutral density created by the injection of the 30L neutral beam and ${\rm d}L$ is the width of the neutral plume formed by the intersection with each sightline. The actual neutral plume is approximately 12 cm wide in the direction normal to injection and is shown to scale in figure 1.

Figure 2 elucidates the range of fast ion velocities that can contribute to the signal for a given LOS and filter pass wavelength—equivalent to a filter selected velocity (v_λ) antiparallel to the LOS. In this figure, α is the angle between the LOS and the local magnetic field at the point of neutralization which occurs in the vicinity of the 30L NB centerline shown in

figure 1. Depending on the phase of gyromotion at the point of neutralization, an ion with velocity components $v_\parallel$ and $v_\perp$ parallel and perpendicular to the magnetic field, respectively, prior to re-neutralization, can undergo a charge exchange, become an excited neutral and emit a Doppler shifted D_α photon with a wavelength matching that of the filter pass wavelength provided that [8]

$$-v_\perp \sin(\alpha) \leqslant v_\lambda - v_\parallel \cos(\alpha) \leqslant v_\perp \sin(\alpha). \tag{1}$$

This inequality simply means that the perpendicular ion velocity component can contribute between $v_\perp \cos(\pi/2 - \alpha)$ and $-v_\perp \cos(\pi/2 - \alpha)$ along the LOS, the exact value of which depends on the phase of motion in the particular gyro-orbit at the time of neutralization. To emphasize the implications of this point, equation (1) only means that it *is possible* for an ion with velocity components $v_\parallel$ and $v_\perp$ satisfying equation (1) to undergo a charge exchange process and emit a D_α photon which is able to pass through the filter. In terms of pitch ($\chi = v_\parallel/|v|$), ion energy (E_i) and filter pass energy (E_λ), this relationship is

$$-(1-\chi^2)^{1/2}\sin(\alpha) \leqslant (E_\lambda/E_\mathrm{i})^{1/2} - \chi\cos(\alpha) \leqslant (1-\chi^2)^{1/2}\sin(\alpha). \tag{2}$$

One consequence is that for a single filter wavelength (not the entire bandpass), the region of a given distribution function that can contribute to the signal goes from an infinitely large area for $\alpha = 90^\circ$ described by

$$E_\mathrm{i}(1-\chi^2) \geqslant E_\lambda \tag{3}$$

to a single curve

$$E_\mathrm{i}\chi^2 = E_\lambda, \tag{4}$$

for $\alpha = 0^\circ$, and viewing parallel to B. For the camera sightlines, α is in the approximate range 20°–40°.

In practice, the lower and upper passband filter wavelengths (or energies) are dependent on position and pixel. This is a consequence of the fact that within the wide field of view, the rays illuminating each pixel do not all pass through the interference filter at the same angle. Any angle (θ) different than normal shifts the center wavelength to the blue according to the well-known formula $\lambda_\mathrm{c}' = \lambda_\mathrm{c}\sqrt{1-\sin(\theta)^2/n_\mathrm{eff}^2}$, where $n_\mathrm{eff} = 1.94$ is the effective index of refraction for the filter. The range of angles and the corresponding lower and upper passband energies (directed antiparallel to the LOS) are shown in figure 3. It should be pointed out that while these are the energies corresponding to the upper and lower passband wavelengths (E_λ from equation (2)), ions with all energies above the lower cutoff can contribute to the signal, a fact that depends on the pitch of that ion velocity according to equation (2). This point will be further clarified later in figure 7 where the result of equation (2) is shown for realistic energies, pitch and sightline trajectories.

Another artifact of the measurement apparatus that must be considered in the following analysis is that mechanical vignetting significantly attenuates signal levels for pixels away from the central region. This attenuation factor has been measured using a uniform intensity light source and an approximate fit is given by

$$V = \exp\left[-\left(\frac{[(x-x_\mathrm{o})^2 + (y-y_\mathrm{o})^2]^{1/2}}{A}\right)^B\right], \tag{5}$$

where $x\,(y)$ is the horizontal(vertical) pixel, $x_\mathrm{o} = 199.3$, $y_\mathrm{o} = 119.9$, $A = 138.8$ and $B = 2.61$. Pixel intensities near the inner and outer wall will be attenuated to approximately 10–20% of the intensity that would be measured in the absence of this effect.

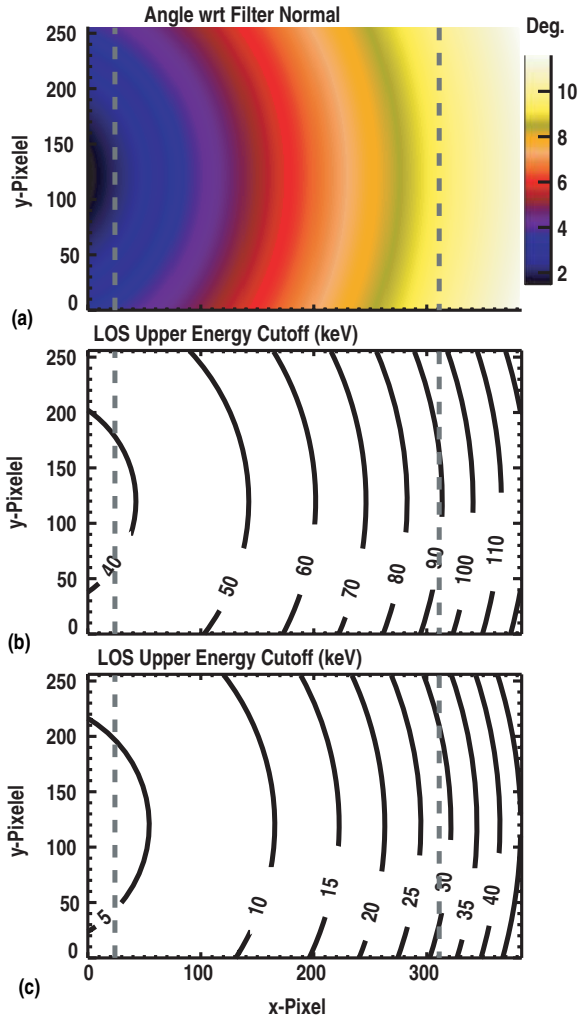

Figure 3. (*a*) Angle with respect to the interference filter normal across the camera field of view. (*b*)/(*c*) Corresponding upper/lower energy cutoff at the knee of the bandpass filter transmission. Energies are for velocities directed antiparallel to the LOS. Vertical dashed lines indicate where the LOS intersects a wall before the 30L NB.

3. FIDAI measurements and modeling

The primary discharge discussed in this paper is a relatively small cross-sectional area, low elongation plasma designed for off-axis neutral beam current drive studies. A representative equilibrium for the primary time range of interest is shown in figure 4(*a*). Overlaid on the equilibrium is the outline of the inner vessel wall as well as the viewing boundary (dashed) defined by the intersection of the edge pixels' lines of sight with the vertical plane defined by the 30L neutral beam injection vector. It is important to point out that some of the extreme left/right lines of sight actually intersect the inner/outer wall before they intersect the 30L NB. This can be seen more clearly by comparison with figure 1. Even with this caveat, however, it is clear that the camera view is capable of covering a large fraction of the plasma cross-section.

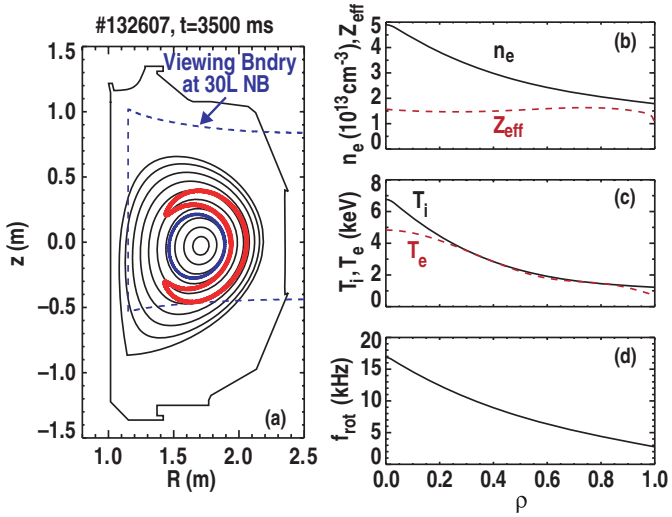

Figure 4. Discharge 132607, $t = 3500$ ms, $B_T = 2.1$ T and $I_p = 0.89$ MA. (*a*) EFIT magnetic equilibrium reconstruction, contours are equally spaced contours ($\delta\rho = 0.1$) of the square root of normalized toroidal flux (ρ). The dashed line indicates the intersection of the edge pixels' lines of sight with the vertical plane defined by the 30L neutral beam injection vector. Red (grey) and blue (black) overlaid curves are typical trajectories of a trapped and counter-passing ion, respectively, that can contribute to the FIDA signal. Particles were initialized with $V_\parallel/V = -0.5$, $R = 1.95$ m, $z = 0$ m, $E = 30$ keV (trapped) and $V_\parallel/V = -0.8$, $R = 1.9$ m, $z = 0$ m, $E = 30$ keV (counter-passing). (*b*) Electron density—solid, Z_{eff}—dashed, (*c*) ion temperature—solid, electron temperature—dashed, (*d*) toroidal rotation frequency.

Also overlaid on this figure are typical trajectories of a trapped and counter-passing particle that can contribute to the FIDA imaging signal. The trapped particle shown can actually only fulfill the condition imposed by equation (1) on the outer leg of its orbit due to the fact that as it precesses around the torus, the particle's pitch oscillates from co-current (inner leg) to counter-current (outer leg). In figures 4(*b*)–(*d*) profiles of electron density (n_e), electron temperature (T_e), ion temperature (T_i), Z_{eff} and toroidal rotation frequency (f_{rot}) are given. The average beam power ($P_B = 3.9$ MW) is modest to reduce instabilities that might enhance fast ion transport over the neo-classical level. The discharge has occasional, relatively weak ($\delta T_e/T_e \approx 12\%$) sawteeth, ELMs and very little Alfvén eigenmode activity.

Shown in figure 5 is the temporal evolution of midplane pixel (202,89) (black) which intersects the 30L NB at $R = 1.90$ m and has a tangency radius of $R_{tan} = 1.77$ m, the same as that of a VBE diagnostic chord [9], also shown in figure 5 (red, labeled VBE). The VBE signal has been scaled to the pixel series after $t = 5200$ ms when NB injection has ceased. The sequence of the 30L NB modulation is displayed in blue and is clearly correlated with increases in the pixel signal level as one would expect since the 30L NB provides the source of injected neutrals (n_{neut}) for charge exchange reactions on the energetic ions. The VBE trace is given to convey the fact that during periods when the 30L NB is turned off, the camera signal returns to a minimum value set very nearly by the VBE. Based on this information it is inferred that VBE is the primary source of non-charge exchange neutral emission, as opposed to other potential sources such as impurity line emission. This finding is consistent with recent FIDA measurements in the blue shifted range [2, 3] on DIII-D. Imaging beam modulation such as this allows an accurate measurement of the background signal levels as a function of time which is useful for isolating the signal coming from FIDA alone.

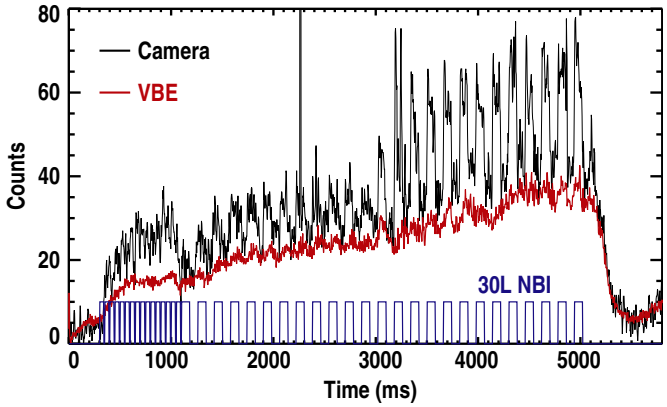

Figure 5. Discharge 132607, midplane camera pixel (202,89) time series (black) and overlaid VBE (red, VBE) measurement from the tangential sightline with the same tangency radius, $R = 1.77$ m. VBE data have been scaled to camera measurement after neutral beam injection turnoff. (Blue) Time history of the 30L neutral beam showing modulation.

The 12-bit camera used is unintensified and the peak signals in figure 5 of approximately 80 counts are out of a possible 4096 (integration time of 1/300 s). An absolute calibration was last done for this diagnostic in 2007 with a different coherent fiber bundle image guide and gives a rough conversion of 3×10^{-9} counts/(photons cm^{-2} sr^{-1}). Unfortunately, the absolute calibration is somewhat unreliable due to neutron degradation and variation of the coherent fiber optic image guide and thus can only be useful to obtain an approximate surface radiance. For all figures that follow which present camera data in counts this conversion factor can be used to obtain order of magnitude estimates for surface radiance values. In principle, the fact the FIDA signal levels appear to be set by VBE is a potentially powerful tool that can be exploited to obtain *in situ* camera calibrations through a calibrated VBE diagnostic or knowledge of the emissivity profile itself from measurements of electron density, temperature and Z_{eff}.

Figure 6 focuses on the time range $t = 3300$–3800 ms, from figure 5. In this time range, the 210R and 30L neutral beams were modulated out of phase as can be seen in figure 6(*c*). Figures 6(*a*) and (*b*) show the 2D FIDA data at time $T1$ and $T2$ before 30L turn-on and immediately after, respectively. Both images are plotted on the same scale and serve to show the 2D change in signal due to charge exchange related emission. Given the results presented in figure 5, figure 6(*a*) is essentially an image of the line integrated VBE profile. Images such as this have been obtained previously and been used to provide 2D profiles of Z_{eff} [10].

The temporal evolution of midplane pixel (172,92) is shown in figure 6(*c*) and displays a behavior fundamental to the validation of this technique as well as the potential information the diagnostic can offer. Phenomenologically, the behavior can be broken into four distinct phases described by looking at times $T1$, $T2$, $T3$ and $T4$. At $T1$, the signal is at some level set by VBE. In the 80 ms time interval preceding this point, the 210R NB was on and serving to build up a population of counter-current going fast ions. At $T2$, the 210R NB has been turned off and the 30L 'neutral source' beam is turned on, causing the signal level to rise. By $T3$ the signal level has decayed significantly and at $T4$ the 30L NB is turned off causing the signal level to return to that set by VBE. To understand this evolution, one must consider that the blue shifted filter acceptance causes the diagnostic to be primarily sensitive to counter-current going fast ions. In these discharges, counter-going fast ions are generated by the 210R NB as

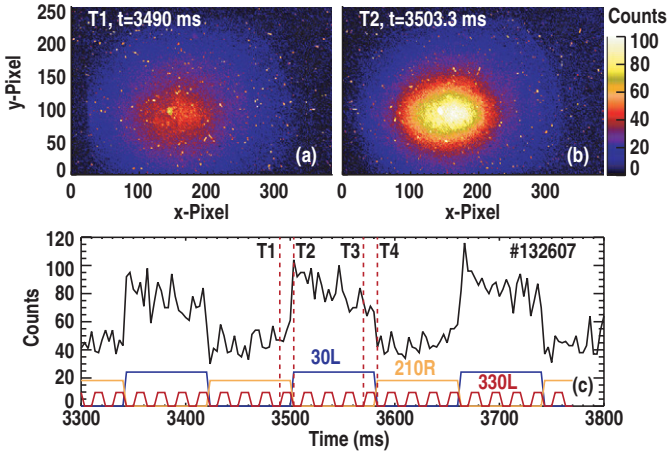

Figure 6. Camera data from discharge 132607 showing the effects of neutral beam modulation. (*a*) Camera data at $t = 3490$ ms when 30L NB is off. (*b*) Camera data at $t = 3503.3$ ms when 30L NB is on. The same scale is used for (*a*) and (*b*). (*c*) Time series of pixel (172,92). The beam modulation cycle is indicated for 30L, 210R and 330L neutral beams. Vertical dashed lines indicate times $T1 = 3490.0$ ms, $T2 = 3503.3$ ms, $T3 = 3570.0$ ms and $T4 = 3583.3$ ms.

well as by pitch angle scattering of other co-injected ions. At $T2$, the time which the imaging beam is turned on, the 210R NB was turned off, thus it is expected that the counter-going fast ion population being measured will begin to diminish on a timescale representative of the classical slowing down time ($\tau \approx 80$ ms). As a result, it is expected that the measured FIDA signal should also decay significantly by $T4$, as is observed.

To quantitatively understand this process, TRANSP [11] modeling of the classical neutral beam deposition was carried out. Shown in figure 7 is the TRANSP calculated fast ion distribution function averaged over the plasma cross-section for times $T2$ and $T3$. From these, it is clear that at $T2$ there is a much larger population of counter-going ($\chi < 1$) fast ions relative to $T3$. Also, it can be seen that a co-going ($\chi > 1$) peak near the injection energy (80 keV) appears at $T2$ due to the turn-on of the 30L NB and by $T3$ this co-going population has filled in a large energy range centered near $\chi = 0.8$. Overlaid on these figures is the approximate lower energy bound permitted by the filter according to equation (2). The camera response will include emission from essentially all regions of velocity space to the right of the lower energy curve. As stated earlier, both passing and trapped particles can contribute to the measured signal. Trapped particles, however, have the subtlety that they will contribute on their counter-going leg, which for these conditions is on the outer leg of their banana orbit. Within the filter acceptance range, the number of fast ions (and expected FIDA emission) has obviously decayed between $T2$ and $T3$.

These distribution functions provide the input to a FIDA modeling code described in [1, 3]. Given an input distribution function, the FIDA code is capable of calculating the full spectrum and theoretical number of photons observed by each pixel and has been adapted to take the array of sightlines for the camera diagnostic as well as to integrate over the appropriate wavelength range for each pixel and include the effects of mechanical vignetting as described by equation (5). The code itself including documentation is available for download [12]. The FIDA diagnostic is a one-dimensional measurement in velocity space, and therefore is theoretically impossible to convert the FIDA spectrum (much less an integral of the emission spectrum over wavelength such as the bandpass filter/camera combination makes) to a fast ion

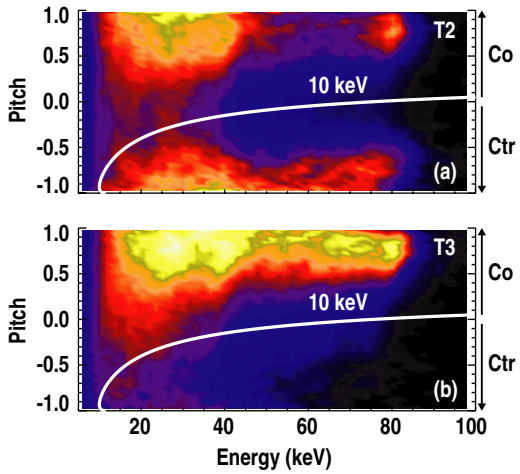

Figure 7. TRANSP calculated distribution functions for (*a*) $T2$ and (*b*) $T3$. Distribution functions are the average of the entire cross-section. The overlaid curve indicates filter acceptance bounds for a representative central pixel energy range. Essentially all ions to the right of the curve can contribute. Curves are calculated according to equation (2).

distribution function [3, 13]. Nevertheless, through forward modeling such as that performed by the FIDA simulation code, one is able to say whether a given distribution function is consistent with measurement.

Results of this modeling and comparison with measurement for time $T2$ are shown in figure 8. Figure 8(*a*) shows the 2D structure of the difference signal between $T2$ and $T1$, equivalent to performing a background subtraction in order to see only the active signal contribution. Figure 8(*b*) shows the result of the FIDA simulation code to be compared with panel 8(*a*). The simulation results have been scaled by a single scaling factor to the experimental measurements where the scale factor was obtained by a least squares fit of the midplane pixel array, the location of which is shown in both panels as a white horizontal line. This scaling and the excellent shape agreement is made clear in figures 8(*c*) and (*d*), where the predicted and the measured signals are compared along a horizontal and vertical line, respectively. Reduced chi-square values are 0.85, 0.99 and 0.77, where the values quoted are for fits to the image, horizontal line and vertical line, respectively. From figure 8 one can see the shape and relative location within the field of view of the experimentally measured FIDA emission is well reproduced by the simulation code.

While this is encouraging, more quantitative information is obtained by investigating the difference between $T3$ and $T2$. Figure 9(*a*) shows the midplane pixel array camera data for times $T1$ through $T4$. By comparison of the $T1$ and $T4$ data, the background signal level is found to remain constant. As shown for a single pixel in figure 6(*c*), figure 9(*a*) shows that the overall signal level is observed to decrease significantly between $T2$ and $T3$ across much of the horizontal pixel array. The FIDA simulation results for times $T2$ and $T3$ along the midplane are shown in figure 9(*b*), where the same scaling factor derived for time $T2$ in figure 8 has been applied to the simulation data for time $T3$. Since the simulation results do not include a background/noise contribution, the relevant quantity to compare is the difference between $T3$ and $T2$. This comparison is made in figure 9(*c*), where the experimental and simulated change in FIDA emission along the horizontal midplane pixel array is shown. It is seen that not only the shape but the quantitative change in FIDA emission due to classical slowing down of

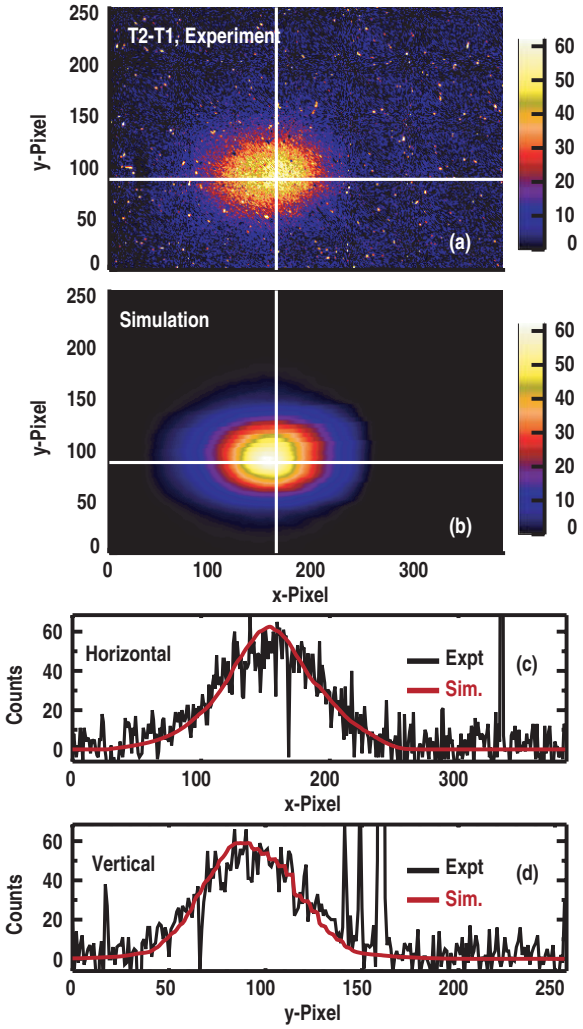

Figure 8. (*a*) Difference of camera measurements at $T2$ and $T1$, i.e. background subtraction to obtain fast ion contribution. (*b*) FIDAI simulation results for the equivalent of panel (*a*). (*c*) Structure along the white overlaid horizontal lines from the surface plots in panels (*a*) and (*b*). Simulation results have been scaled by a single constant to experimental measurements along this line. (*d*) Structure along the vertical line in panels (*a*) and (*b*), the same scaling factor was used as in (*c*).

the counter-going fast ions is reproduced by the simulation. Reduced chi-square values from comparison of simulation results with data at time $T3$ are 0.93, 0.89 and 1.07, where these values correspond to fits to the image, horizontal line (fit shown) and vertical line, respectively.

Despite the fact that the camera calibration is not well known, further quantitative comparison can be made with FIDA simulation predictions through comparison with VBE. Theoretically, the VBE is easily calculated using profiles of n_e, T_e and Z_{eff}—the line integrated bremsstrahlung emissivity is an output of the FIDA simulation code. By plotting the ratio of the FIDA signal to the VBE one can essentially remove the unknown camera calibration. Figure 10 shows a comparison of the measured FIDA signal at $T2$ (that from figure 8(*b*))

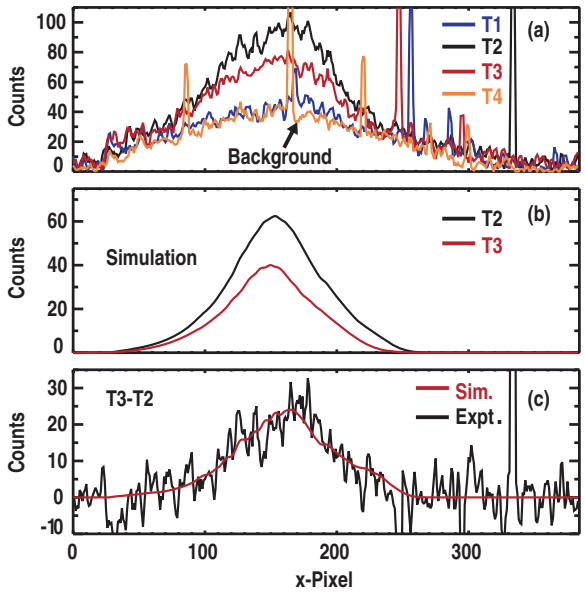

Figure 9. Radial structure along the horizontal line from figure 8(*a*) for times $T1$ through $T4$. The background level obtained at $T1$ and $T4$ is pointed out. (*b*) FIDAI simulation results for $T3$ and $T4$ along the same line as (*a*). Both use the same scaling constant derived from figure 8(*a*). (*c*) Experimental and simulated difference in the signal between times $T3$ and $T2$ due to slowing down of the counter-going fast ions.

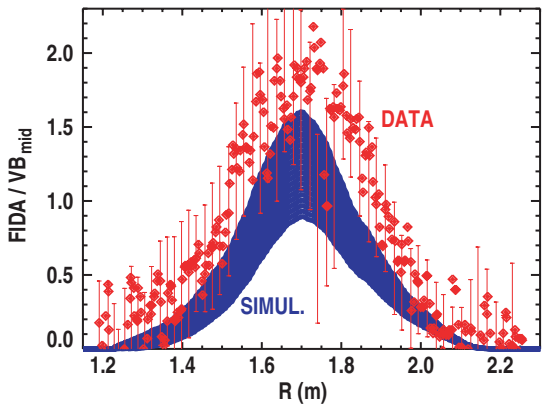

Figure 10. Experimental (DATA) and Simulated (SIMUL.) FIDA signals along the device midplane at time $T2$ when scaled to the signal due to visible bremsstrahlung on the sightline with tangency radius $R = 1.985$ m (VB_{mid}). Every 5th error bar is plotted for reference. Scaling to line integrated VBE is used to remove unknown camera intensity calibration.

with that predicted by the FIDA simulation code, where the FIDA profiles have been scaled by the measured and predicted VBE signal from a mid-radius sightline, respectively (VB_{mid}). The measured VB signal was obtained by assuming all emission at $T1$ was due to VBE. The value at mid-radius was chosen because the inner density profile in DIII-D has relatively large error bars, which further complicates the comparison and can cause large errors in

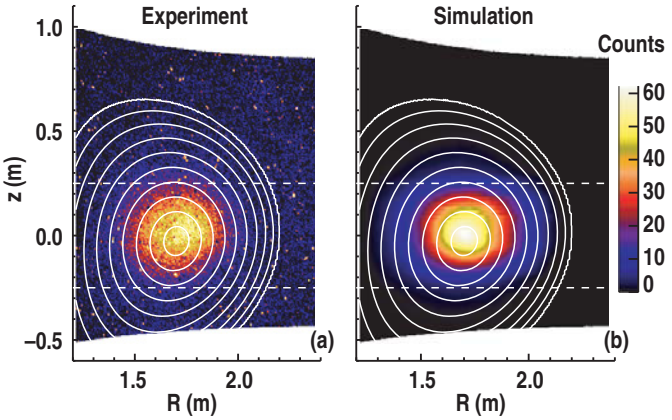

Figure 11. Experimental (a) and simulated (b) FIDAI data from figure 8 plotted using R, z coordinates at which sightlines intersect the vertical plane defined by the 30L neutral beam injection vector. Overlaid ρ contours are calculated at the same R, z locations. Experimental data is the camera image at $T2$ minus that at $T1$. Horizontal dashed lines indicate the $1/e$ extent of the neutral density plume.

calculating the predicted ratio; this scaling is particularly sensitive to density errors since visible Bremsstrahlung increases as n_e^2 and the FIDA signal scales roughly as $1/n_e^2$ [3]. When plotted in this way, it can be seen that the FIDA simulation code predictions for the shape *and level* of FIDA emission are in reasonable quantitative agreement with measurement. However, it appears that the data in the center are somewhat systematically higher than the predictions, a fact which can easily be reconciled by a small decrease in density (≈5–10%).

To lend a sense of size-scale to the 2D images, as well as the relative centering with respect to the plasma, the 2D experimental and simulated data from figure 8 are plotted in the R, z coordinates (figure 11). The actual coordinates chosen correspond to the point of intersection between each pixel sightline and the vertical plane described by the 30L NB injection centerline (as shown in figure 4(a)). Overlaid on these figures are equally spaced contours ($\delta\rho = 0.1$) of the square root of normalized toroidal flux (ρ). Also shown in figure 11 is the vertical extent of the injected-neutral beam where the $1/e$ density points of the neutral plume are represented by dashed white lines. As stated earlier, the small almost circular plasmas used in this study were developed for off-axis neutral beam current drive experiments, an analysis of which will include FIDA imaging data and will be presented in future publications.

Figure 11 shows that the vertical extent of the FIDA emission is largely determined by the height of the neutral beam. One might ask what determines the shape and extent in the radial direction. As discussed briefly in section 2, neglecting charge exchange cross-section effects, the FIDA emission is given roughly by the product of $n_{fi} n_{neut} V \, dL$, where n_{fi} is the fast ion density in the region of velocity space being imaged, n_{neut} is the neutral density, dL is the path length along the line of sight set by the intersection with the 30L neutral beam and the attenuation due to vignetting has been added by the V. Figure 12 shows camera data along the equivalent of the $z = 0$ line in figure 11(a), as well as n_{fi} from TRANSP, n_{neut} from the FIDA simulation code and the camera vignetting attenuation function V from equation (5). The fast ion density is evaluated for counter-going ions with energies greater than 10 keV, similar to the region of velocity space for which the camera is sensitive. From this figure, it is obvious that the fast ion density profile determines the width the horizontal direction and the location of the peak is a result of the convolution with the neutral density profile which has an

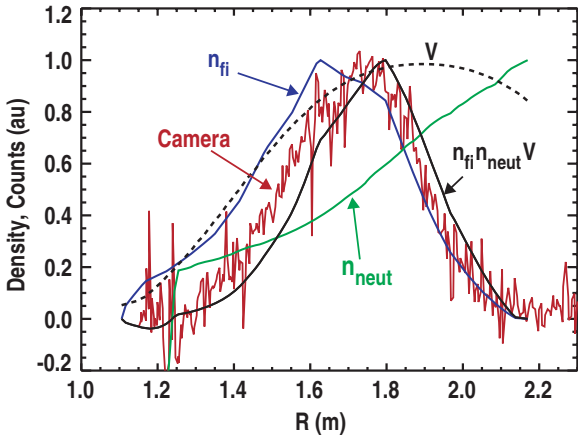

Figure 12. Radial profile of the midplane camera data at the start of the 30L turn-on (equivalent to $T2$–$T1$) averaged over five repetitive cycles of beam injection (red). Counter-going fast ion ($E > 10$ keV) density profile from the TRANSP (blue, $n_{\rm fi}$). Neutral density profile from the FIDA simulation code (green, $n_{\rm neut}$). Camera vignetting attenuation function (dashed, V). Fast ion density profile multiplied by the neutral density profile and the vignetting function (black, $n_{\rm fi}n_{\rm neut}V$). All profiles are normalized.

exponential decay with penetration depth. The agreement of the camera data with the simple $n_{\rm fi}n_{\rm neut}$ estimate of the signal is extremely encouraging as it offers the possibility for readily obtaining rough fast ion profile shapes with minimal calculation—all that is needed is an estimate for the neutral density profile. Fast ion profile data obtained by taking FIDA emission measurements integrated over wavelength (such as those here) divided by the neutral density profile are what has been termed 'FIDA density' in several recent publications [14, 15]. As stated previously, while it is not possible to invert the FIDA data to obtain the full distribution function, it is extremely useful to have an estimate such as this. For example, 'FIDA density' profiles obtained in this way are useful for comparing the relative differences between similar discharges with varying levels of MHD activity or other non-ideal effects.

4. Spectrometer based vertical FIDA measurements

The 2D FIDA imaging measurements and simulations presented here extend and also help to validate the original spectrometer based FIDA system on DIII-D. One large asset of the vertical system is that the full spectrum is recorded as opposed to just integrated power in some wavelength band as with the camera pixels. Measurements as well as modeling of the full spectrum in the D_α range can be invaluable in helping to determine the relative magnitudes of the separate contributions to the signal.

In figure 13(a) the measured spectrum from a vertically viewing spectrometer chord at $R = 1.96$ m with and without the neutral source beam (330L in this case) is shown, corresponding to a time near $T2$ and $T1$, respectively. The bright central portion of the spectra are attenuated by an OD3 neutral density filter, which is a change from the original instrument that utilized an opaque blocking bar [2]. The effect of the relatively broad instrument response function on the narrow oxygen V (650.3 nm) and cold D_α lines (656.1 nm) is apparent. Figure 13(b) shows the measured spectrum from figure 13(a) after background subtraction (blue) compared with theoretical predictions of the FIDA (green), thermal-neutral

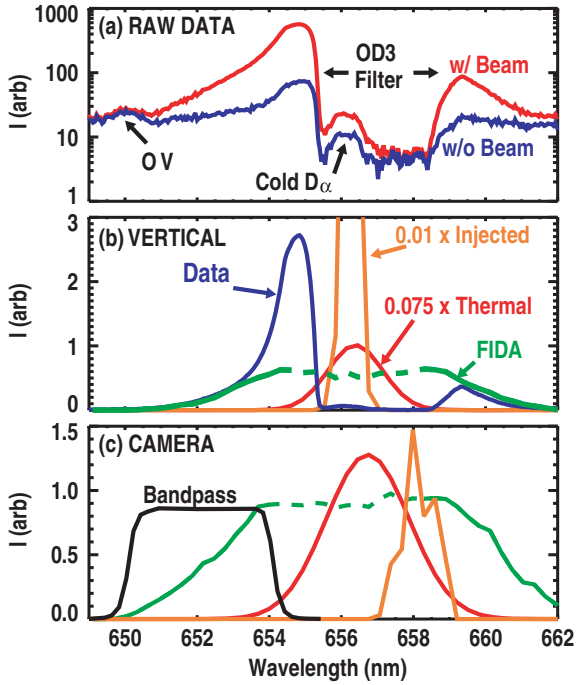

Figure 13. (*a*) Spectra measured when the viewed beam is on (red) and off (blue) by the vertically viewing spectrometer from the channel at $R = 1.96$ m [2]. The bright central portion of the spectra is attenuated by an OD3 neutral density filter. The effect of the relatively broad instrument response function on the narrow oxygen V (650.3 nm) and cold D_α lines (656.1 nm) is apparent. (*b*) Measured spectrum after background subtraction (blue), theoretical predictions of the FIDA (green), thermal-neutral (red) and injected-neutral (orange) light for the vertically viewing channel at $R = 1.96$ m. The FIDA prediction is invalid near the center wavelength (dotted line). The nominal interference filter band for a 5° tilt angle is also shown (black). (*c*) Theoretical predictions for a camera pixel that intersects the imaging beam near the magnetic axis (150,94).

(red) and injected-neutral (orange) light for the vertically viewing channel at $R = 1.96$ m. Because the FIDA simulation code cuts off the fast ion distribution function at low energies (approximately 8 keV), the FIDA prediction is invalid near the center wavelength (dotted line). As previously observed in MHD-quiescent plasmas [3], for large Doppler shifts, the spectral shape is in excellent agreement with the simulation. At lower Doppler shifts, the comparison is complicated by the finite instrument response function and the effect of the central neutral density filter. Estimates indicate that injected-neutral light contributes to the measured spectra for the vertical viewing system at 654.5 nm.

Figure 13(*c*) shows the theoretical prediction for the various contributions to the D_α spectrum of a FIDAI camera pixel that intersects the imaging beam near the magnetic axis (150,94). The bandpass filter is at an angle of 5.3° for this pixel and its nominal passband is shown (purple). From figure 13(*c*) several things are apparent. Due to the relatively large angle between the sightlines and the 30L imaging beam, the direct emission from injected neutrals has a significant red Doppler shift making it peak around 657.7 nm and thus does not contribute to the measured signal. Due to the relatively wide filter bandpass, however, halo D_α emission from neutralized thermal ions is expected to contribute slightly to the measured signal at this location. At other locations with larger filter angles and lower T_i, this effect is

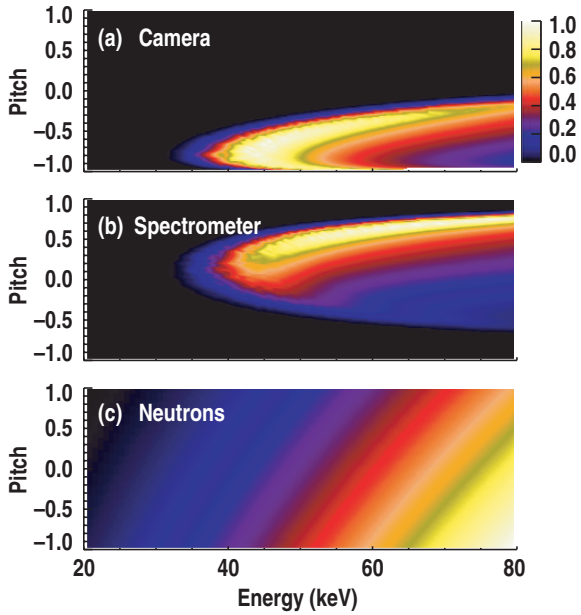

Figure 14. Weight functions $W(E, \chi)$ on a linear scale for (a) a tangential camera view for $E_\lambda = 40$ keV, (b) a vertical spectrometer view also for $E_\lambda = 40$ keV and (c) the beam-plasma neutron rate. The weight functions are based on the approximations described in the appendix of [8].

less pronounced. Figure 13(c) also shows that the restriction of the FIDA simulation code to ions with energies greater than 8 keV (corresponding to $\lambda \approx 653.8$ nm in figure 13(b) and $\lambda \approx 654.4$ nm in figure 13(b)) will artificially reduce the number of FIDA photons in the filter passband, an effect which is estimated to be on the order of 5–10% depending on the filter angle.

As mentioned, because of its tangential viewing geometry (figure 1) and the bandpass filter that measures blue shifted light, with the standard DIII-D plasma current direction, the camera views detect primarily counter-current circulating beam ions. The sensitivity of a fast ion diagnostic in velocity space is conveniently characterized by a velocity-space weight function, $W(E, \chi)$, where the measured signal S is the integral of the convolution of the weight function with the fast ion distribution function $F(E, \chi)$, $S = \int W(E, \chi)F(E, \chi)\,\mathrm{d}E\,\mathrm{d}\chi$ [8]. The weight function for a typical camera view at a particular wavelength ($E_\lambda = 40$ keV) is shown in figure 14(a), which closely follows the curves shown in figure 7, with the greatest sensitivity at the low-energy limits of the curves due to an increased cross-section for the charge exchange reaction. This can be seen in figure 15 where the relevant charge exchange cross-sections between a neutral deuterium atom and a fast deuteron are given [16]. After bandpass filtering over all detected wavelengths, the weight function of the camera strongly favors counter-circulating fast ions with large negative pitch ($\chi \approx -1$). In contrast, the vertically viewing spectrometer detects FIDA emission with a weight function that is more balanced in pitch sensitivity yet slightly favors co-circulating ions (figure 14(b)). Similarly, the neutron rate (which is theoretically ∼75% beam–plasma and ∼25% beam–beam emission for these conditions) also detects fast ions from all of phase space, with a weight function that favors high energies and slightly favors counter-circulating ions (figure 14(c)).

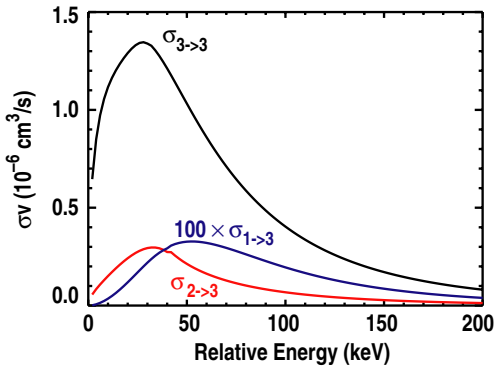

Figure 15. Charge exchange cross-sections multiplied by relative velocity (σv) for the charge exchange between a deuteron and a deuterium neutral in the $n = 1, 2$ and 3 excited states resulting in a fast neutral in the $n = 3$ excited state as a function of relative energy [16]. Note, the $1 - >3$ cross-section is multiplied by a factor of 100.

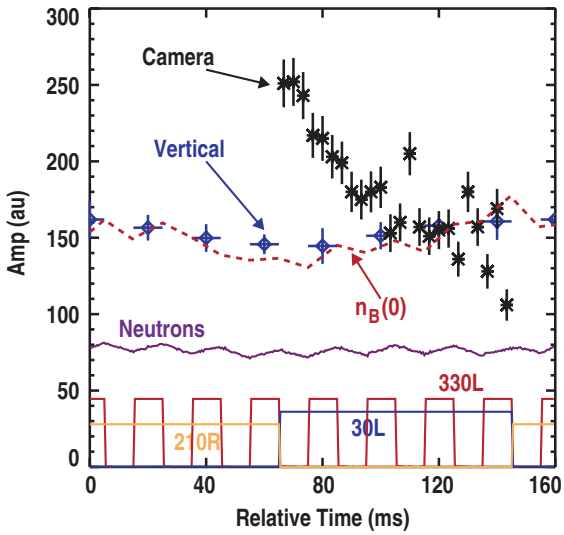

Figure 16. Time evolution of fast ion signals after averaging over five repetitive cycles of beam injection. The camera data (counts) are for a central pixel (172,92) with the average background when 30L is off subtracted; the error bars are from counting statistics. The vertical data (au) are for the $R = 180$ cm spectrometer channel after integrating over wavelengths that are transmitted by the bandpass filter; the error bars are from the standard deviation of the five nominally identical cycles. The trace labeled '$n_B(0)$' is the central beam density computed by TRANSP; the trace times 5e10 gives the density in cm^{-3}. The trace labeled 'Neutrons' is the volume-averaged neutron rate from a plastic scintillator in units of $10^{13}\,\mathrm{n\,s}^{-1}$. The timing of the various neutral beam sources is also indicated.

The different sensitivities of the various fast ion diagnostics result in quite different responses to changes in the fast ion distribution function when the beams are modulated, a fact that is highlighted in figure 16. As noted earlier, the camera FIDA signal (which is only available when 30L is on) is largest just after the counter-source turns off and steadily decays as the counter-population (created primarily by injection of the 210R beam) is replaced by

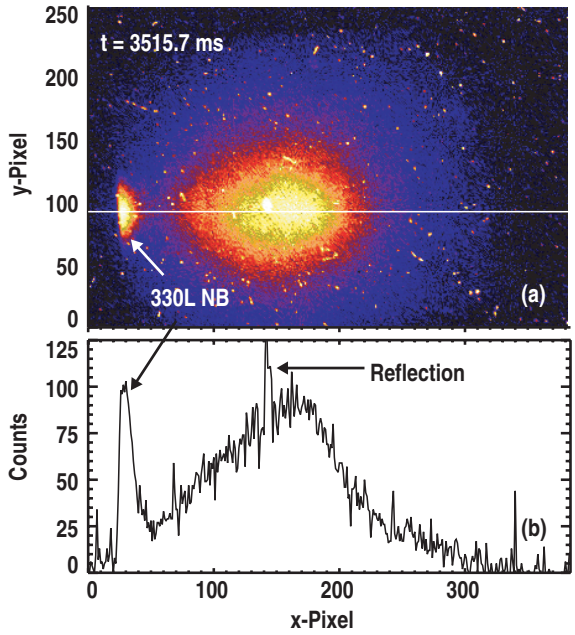

Figure 17. Camera data from discharge 132607 at $t = 3515.7$ ms. Emission from excited neutrals injected by 330L NB and reflected emission from 210R injected neutrals is pointed out.

the co-going population. In contrast, the changes in the neutron and vertical FIDA signals are modest. Because of its sensitivity to the highest-energy ions, the neutron rate rises (decays) each time 330L turns on (off) but is nearly constant on average. The vertical FIDA signal decreases slightly during counter-injection and rises during co-injection but, because vertical views are sensitive to all of velocity space, the changes are modest. The vertical FIDA signal closely follows the central beam density predicted by TRANSP, a tendency that was previously noted in other MHD-quiescent discharges [3]. The marked differences in time evolution of these different fast ion signals are consistent with the expectations from figure 14, confirming our interpretation of the camera signals as FIDA light from counter-circulating fast ions.

5. Additional discussion

The interference filter used does not allow red shifted D_α emission from 30L injected neutrals to contribute to the camera signal. The same is not true, however, for blue shifted D_α emission from 330L injected neutrals and reflected emission from 210R neutrals. From figure 1 one can see that the 330L neutral beam is within the camera's field of view on the extreme left side, some of which is interrupted by the inner wall. This emission can be seen in figure 17 where the timestep shown corresponds to a time when the 330L, 210R and 30L neutral beams were on. Blue shifted D_α emission from the 330L injected neutrals is pointed out as well as another anomalous spike in the image near x-pixel $= 140$ (figure 17(b)). This spike labeled 'reflection' in figure 17(b) is a result of blue shifted D_α emission from 210R injected neutrals that has been reflected by a polished object on the wall. The source of this emission was determined conclusively by temporal correlation with 210R modulation. Since beam viewing

dumps are impractical for wide-angle imaging, reflected signals such as this highlight the need for a thorough analysis of all possible sources that can contribute to the inferred FIDA signal. Although it places constraints on the imaging of dynamic changes to the FIDA emission, non-ideal effects such as reflections can be greatly minimized with appropriate imaging beam modulation and background subtraction techniques. Alternatively, it has been observed that the small gaps between carbon tiles on the inner wall of DIII-D serve as relatively good viewing beam dumps. Thus, these tile gaps can be used to determine the relative importance of reflections to the total overall signals levels as well as to provide a much coarser set of image points at which the effects of reflections and other such sources will be reduced.

6. Summary and conclusions

In summary, temporally resolved 2D measurements of D_α emission produced by neutralized fast ions born in charge exchange events with injected neutrals and halo neutrals have been presented. The technique FIDAI utilizes a fast framing camera in conjunction with a narrowband interference filter centered in the blue shifted D_α wavelength range to preferentially select emission from energetic neutrals. Both the spatial structure and the temporal evolution of the imaged FIDA emission, during a specifically designed FIDA/FIDAI validation experiment, are in excellent agreement with Monte Carlo simulations. By making use of a camera's multipixel CMOS chip, the need for a channel to channel spatial calibration is eliminated (or reduced) relative to previous stand alone individual channel FIDA systems that each rely on individual detectors. This technique can be used to obtain 2D information about the underlying fast ion population in fusion plasmas and, in particular, the response to events such as RF heating [8] and redistribution caused by MHD and strong Alfvénic activity [14, 15].

Future work will include an analysis of the same discharge presented here at an early timestep in which the plasma was shifted downward to obtain off-axis neutral beam current drive [17]. Additionally, it is expected that with relatively minor modifications the system could be made to image several wavelength bands on the same CMOS chip. Such an improvement would allow simultaneous 2D measurements of separate energy ranges as well as VBE in a comparable wavelength region free of D_α emission.

Interestingly, although not directly relevant to FIDA measurements, it is pointed out that the use of a red shifted filter would permit emission from the 30L injected neutrals to enter the camera. The result would be a camera based wide-angle equivalent to the beam emission spectroscopy (BES) system on DIII-D, which at full framerate would have a 120 kframes s^{-1} bandwidth.

Acknowledgments

This work was supported by the US Department of Energy under DE-FC02-04ER54698, SC-G903402 and DE-FG02-07ER4917. The authors would like to thank Drs R L Boivin, N H Brooks, D Liu, G R McKee, R Nazikian, M Podestá, E Ruskov, W M Solomon and M R Wade for a range of contributions from useful discussions to hardware and simulation code development. Also, M Murakami, J M Park and the DIII-D team are acknowledged for facilitating the dedicated experimental time focused on validation of this diagnostic. Charge exchange cross-section data are obtained from the Atomic Data and Analysis Structure (ADAS) compilation. The originating developer of ADAS is the JET Joint Undertaking.

References

[1] Heidbrink W W, Burrell K H, Luo Y, Pablant N A and Ruskov E 2004 *Plasma Phys. Control. Fusion* **46** 1855
[2] Luo Y, Heidbrink W W, Burrell K H, Kaplan D H and Gohil P 2007 *Rev. Sci Instrum.* **78** 033505
[3] Luo Y, Heidbrink W W, Burrell K H, Ruskov E, Solomon W M 2007 *Phys. Plasmas* **14** 112503
[4] Podestá M, Heidbrink W W, Bell R E and Feder R 2008 *Rev. Sci. Instrum.* **79** 10E521
[5] Yu J H *et al* 2008 *Phys. Plasmas* **15** 032504
[6] Van Zeeland M A *et al* 2008 *Nucl. Fusion* **48** 092002
[7] Yu J H, Van Zeeland M A and Chu M S 2008 *Rev. Sci. Instrum.* **79** 10F516
[8] Heidbrink W W, Luo Y, Burrell K H, Harvey R W, Pinsker R I and Ruskov E 2007 *Plasma Phys. Control. Fusion* **49** 1457
[9] Schissel D P, Stockdale R E, St. John H E and Tang W M 1988 *Phys. Fluids* **31** 3738
[10] Patel A, Carolan P G, Conway N J and Akers R J 2004 *Rev. Sci. Instrum.* **75** 4944
[11] Budny R V 1994 *Nucl. Fusion* **34** 1247
[12] https://webfiles.uci.edu/eruskov/FIDAcode_distribution/
[13] Egedal J and Bindslev H 2004 *Phys. Plasmas* **11** 2191
[14] Heidbrink W W *et al* 2007 *Phys. Rev. Lett.* **99** 245002
[15] Van Zeeland M A *et al* 2008 *Plasma Phys. Control. Fusion* **50** 035009
[16] Atomic Data and Analysis Structure (ADAS) compilation. *ADAS*, http://adas.phys.strath.ac.uk
[17] Park J M *et al* 2008 *Phys. Plasmas* Submitted